Deformation of a two-dimensional viscoelastic drop at non-zero Reynolds number in time-periodic extensional flows

Kausik Sarkar, William R. Schowalter*

Department of Chemical Engineering, University of Illinois at Urbana-Champaign, Urbana, IL 61801, USA

Abstract

The kinematics of a potential vortex offers an interesting flow history for a rheologically complex material, and earlier work on that subject led us to consider the behavior of a Newtonian drop in three related time dependent flow fields [K. Sarkar, W.R. Schowalter, Deformation of a two-dimensional drop at non-zero Reynolds number in time-periodic extensional flows: numerical simulation, J. Fluid Mech., 2000, submitted for publication; K. Sarkar, W.R. Schowalter, Deformation of a two-dimensional viscous drop in time-periodic extensional flows: analytical treatment, J. Fluid Mech., 2000, submitted for publication]. In the work reported here the drop, characterized by an upper-convected Maxwell model (UCM), is suspended in an incompressible Newtonian fluid. Again, three related flows are considered. The first is that of a potential vortex, modeled by an extensional flow field near the drop with rotating axes of stretching. The second is a generalization of the first and is called *rotating extensional* (RE) flow, in which the frequency of revolution of the flow is varied independently of the shear rate. Finally, we consider *oscillating extensional* (OE) flow.

Calculations were performed at small but non-zero Reynolds numbers using an ADI front-tracking/finite difference method. We have developed an analytic elastic-viscous stress splitting scheme obtained by an integration by parts of the constitutive equation. The scheme explicitly separates the diffusive part of the momentum equation for a wide range of differential constitutive relations. An ADI implementation is executed for the diffusive part. We investigate the effects of periodicity, Reynolds number and relaxation time on the drop dynamics. For a vortex and an RE flow, the long-time deformation reaches a steady value, and the drop attains a revolving, steady elliptic shape. The long-time values of deformation show complex non-monotonic behavior with variation in Weissenberg number, an effect of the decreased damping and increased elasticity, as well as the presence of a shear wave triggered by the UCM constitutive relation. The first two effects are modeled successfully by a simple ODE presented in Appendix A. The wave effects are briefly discussed in Appendix B. © 2000 Elsevier Science B.V. All rights reserved.

Keywords: Drops; UCM; Potential vortex; Extensional flow; Time-dependent

* Corresponding author. Fax: +1-21-7444-7705.

1. Introduction

Drop deformation is relevant to a number of industrial, biological and environmental processes. These include formation of emulsions, dynamics of multi-phase flow heat transfer, mixing, and structure formation in polymeric blends. The drops are deformed, torn apart, and coalesced together giving rise to a time dependent size and shape distribution with complex rheological response for the overall flow. Computational simulation of such a flow is a challenging task. It can be better appreciated by noting that a consistent mathematical description, even of a single drop, is a difficult non-linear moving-boundary problem with boundary conditions prescribed on a surface that is determined only as a part of the solution.

Taylor initiated a systematic study of the drop deformation process with experiments and analysis with the four-roll mill apparatus [3–5]. Since then sustained research effort has resulted in significant gain in knowledge about the phenomenon and its effect on emulsion rheology (see [6] for a review). A variety of linear flows combining stretching and rotation has been studied for the effect on deformation. This has led to classifications such as strong and weak flows depending on the deformation they cause [7,8]. However, the classification is based on the gradient of the flow, and is valid only for motions with constant stretch history (MCSH). Astarita [9] provided a criterion for general unsteady flows. These criteria fail to take account of the effects of the drop on the flow. Incorporation of dynamics was attempted by Olbricht et al. [10], who studied evolution equations for representative micro-variables of deformation. Szeri et al. [11] introduced time varying flow, and investigated the resultant non-autonomous dynamical system. The criteria emerging from their work went beyond a linear stability analysis for the initiation of stretching, and encompassed information about global dynamics. Most of these theoretical explorations were supported by experiments performed with an improved computer-controlled four-roll mill developed by Bentley and Leal [12,13].

Deiber and Schowalter [14] have suggested the potential vortex as a useful base flow to study microrheological behavior. In this flow a drop or a blob of polymer experiences a time-dependent non-viscometric stretching that provides an interesting point of departure from the four-roll mill or the Maxwell orthogonal rheometer. A potential vortex can provide pertinent information not accessible through a four-roll mill but relevant to turbulent flow of an emulsion or a polymeric solution. Furthermore, approximate experimental realization of a potential vortex is possible [15,16]. We have initiated a numerical analysis of a drop deforming in such a potential vortex and other related flows. Analysis for a Newtonian flow has recently been completed [1,2] for two-dimensional drops that exhibited interesting resonance phenomena. Here we continue our effort with a non-Newtonian drop.

Most studies to date of drop deformation have been restricted to linearized Newtonian Stokes flow due to the small Reynolds number (small size) of the drops. For the viscous case semi-analytic methods at the limit of small deformation [6,17], or boundary-element methods for large deformation [18] have been applied to solve the problem. Following our Newtonian study [1], we adopt here a finite Reynolds number computational strategy using front-tracking/finite difference method developed by Tryggvason et al. (see, e.g. [19–21]). The front-tracking method offers generality over boundary elements and computational advantages over finite elements/differences with a body fitted mesh. A drop suspended in a vortex is a three-dimensional problem. As an initial effort we have restricted ourselves to a two-dimensional case, thereby making the drop an infinite cylinder. Due to the satisfying analytical support found for our earlier two-dimensional calculations [1,2], we believe that the rich physics shown here for two dimensions is qualitatively correct also for three dimensions. A time splitting ADI scheme has been used to achieve low but non-zero Reynolds number (the lowest Reynolds number treated here is 0.1).

The literature of non-Newtonian flow computation is much more recent in comparison to its Newtonian counterpart. Early attempts soon uncovered notorious convergence difficulties relating to geometric and constitutive singularities, as well as the so-called high Weissenberg number problem. The source of the problem has been recognized as partially due to change of type of equation from elliptic to hyperbolic, driven by numerical error [22,23]. Since the late eighties extensive numerical experimentation with different algorithms and theoretical analysis has led to the development of a number of finite element schemes such as elastic-viscous stress splitting (EVSS), explicitly elliptic momentum equation (EEME), stream-wise upwinding Petrov–Galerkin (SUPG), streamline finite element (SFEM), and discrete Galerkin (DG) that are able to handle the numerical difficulties [24–28]. Attempts have been made to incorporate the advantages of different methods through consolidation, e.g. DAVSS-G/DG by Sun et al. [29].

Recently a number of researchers [30–34] have successfully applied staggered grid finite volume methods such as the SIMPLE family [35] to viscoelastic problems. Staggered grid provides a desirable coupling between velocity and the stress variables. Oliveira et al. [36] have successfully applied a collocated (non-staggered) finite volume method, using special treatment to preserve the stress–velocity coupling.

Most of the extant numerical efforts have been aimed at simple, steady, two-dimensional/axisymmetric benchmark problems such as flow through a sudden expansion or around a sphere in a pipe. The work of Mompean and Deville [37] is a notable exception, simulating unsteady, three-dimensional simulation of an Oldroyd-B fluid through a planar contraction. Non-Newtonian multi-phase computation for drop deformation has been performed by Bonsfield et al. [38], Ramaswamy and Leal [39,40] and Toose et al. [41] in steady extension flows. Bousfield et al. performed an axisymmetric Galerkin/finite element analysis of a bubble suspended in on Oldroyd B fluid. Ramaswami & Leal applied a body-fitted orthogonoll mesh to a drop of Ckilcot-Rallison fluid. Toose et al. used a boundary-intergral method with discritized volume integration for the extra stress contribution to a two-dimensional Oldroyd-B drop. steady axisymmetric extension of a drop of Chilcot–Rallison fluid. The latter used a boundary-integral method with discretized volume integration for the extra stress contribution to a two-dimensional Oldroyd-B drop deforming in a steady extensional flow.

It has been recognized that simple viscoelastic models like the single mode UCM is not adequate for realistic rheological response. However, the UCM with its severe numerical difficulties is preferred for developing robust numerical schemes that are then expected to perform well with other models. We too have chosen the UCM with a single relaxation time as a model equation for our computation.

As mentioned above, one of the primary aims of the work is to investigate vortex flow kinematics in drop deformation. However, the linearized vortex model is a special case of more general rotating extensional (RE) flows, where the axes of stretching are rotating with time. These flows along with oscillating extensional (OE) flows have been described in detail in [1,2]. The importance of extensional flows in drop deformation that are investigated here have been noted by Taylor — a very viscous drop that would reach an equilibrium shape in a steady shear with an arbitrarily large shear rate would extend continuously in a two-dimensional extensional flow, once the rate exceeds a critical value.

Sections 2–4 describe the mathematical formulation of the problem and its numerical implementation. The results are presented for three different Reynolds numbers in Section 5. In Section 6 we summarize our findings. Appendices A and B describe, respectively, a simple one-dimensional model for drop deformation and the effect of shear wave propagation. The latter is essential for understanding the numerical results.

Although the physical problem and the results are distinct from our earlier work, the computational methodology is similar to that employed in [1]. In order to provide a self-contained description of the present work, Sections 2–4 draw heavily on our earlier publication. The reader familiar with that paper may wish to proceed directly to Section 4.2.1.

2. Vortex flow and other time-dependent flows

We describe here the kinematics of potential vortex flow with respect to individual fluid elements or embedded drops or polymer blobs. As a fluid element in a potential vortex revolves, there is no rotation about the origin of the vortex and the principal axes of stretching rotate about the center of the element, as shown in Fig. 1. It is instructive to compare this drop behavior with that in other well-known time-periodic flows, such as oscillatory shear flow and oscillatory extensional flow (with an invariant axis of extension). The behavior of a drop in each of these flows is compared in Fig. 2. In potential vortex flow, the drop does not rotate, due to absence of vorticity, as it follows a periodic path around the vortex. However, the flow is distinctly different from oscillatory extensional flow, where axes of extension and contraction are always along lines 1–3 and 2–4, alternatively. In the case of the vortex, the axes rotate, and hence the maximum stretching takes place at time-varying locations along the drop interface.

In our analysis a linearization approximation is used. Hence, a drop in a vortex is, at any instant, subjected to a pure extensional flow, but the principal axes of extension rotate (Fig. 1). In our numerical simulation the vortex field is represented by such a linear rotating extensional flow, and there is a definite relationship between the shear rate of the flow and the frequency. However, this linear approximation to the vortex field also permits a more general flow field — namely a rotating extensional flow with independently varying shear rate and frequency. We have studied drop deformation in this flow as well as in an oscillating extensional flow (Fig. 2b).
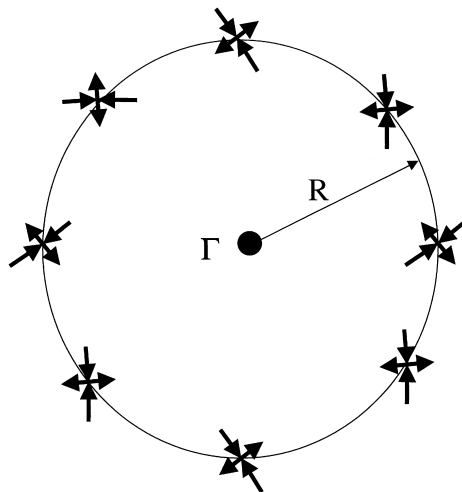
Fig. 1. Velocity gradient in a potential vortex (from [1]).
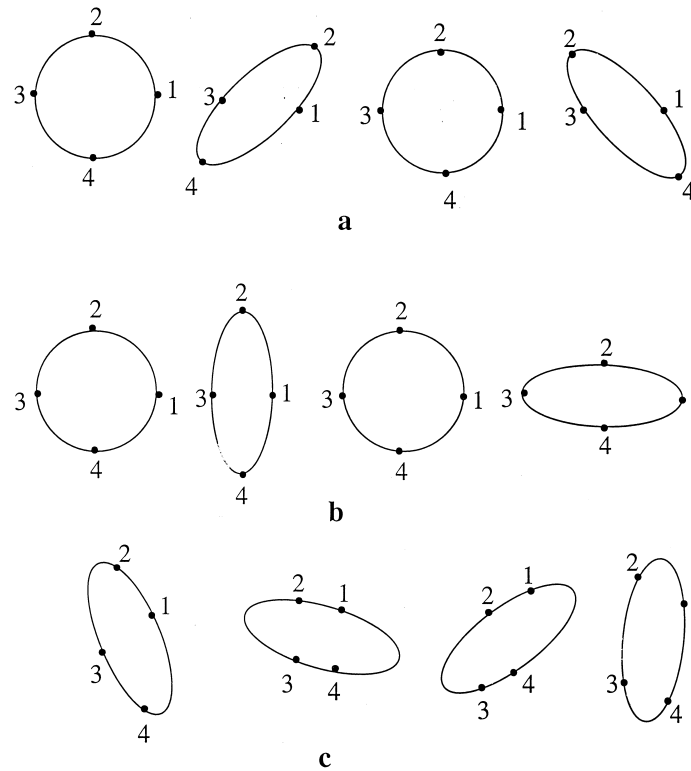
Fig. 2. Drop in different time-periodic linear flows: (a) oscillatory shear flow, (b) oscillatory extensional (OE) flow, and (c) vortex/generalized rotating extensional (RE) flow (from [1]).

3. Mathematical formulation

3.1. Governing equations

The velocity field $\boldsymbol{u}$ and the pressure p satisfy the equation of momentum conservation

$$\frac{\partial(\rho\boldsymbol{u})}{\partial t} + \nabla \cdot (\rho\boldsymbol{uu}) = -\nabla p + \int_{\partial B} \mathrm{d}\boldsymbol{x}_B \kappa \boldsymbol{n}\sigma \delta(\boldsymbol{x} - \boldsymbol{x}_B) + \nabla \cdot \tau, \tag{3.1}$$

in the entire domain Ω, consisting of the continuous fluid domain Ω_c and the suspended drop Ω_d with appropriate boundary conditions at the outer boundary $\partial\Omega$ (Fig. 3). Here σ is the interfacial tension, ∂B is the surface of the drop consisting of points $\boldsymbol{x}_B$, κ the local curvature, $\boldsymbol{n}$ the outward normal to the surface, and $\delta(\boldsymbol{x} - \boldsymbol{x}_B)$ is the (two-dimensional for the present 2D problem) Dirac delta function. The deviatoric stress tensor τ for an incompressible Newtonian fluid in Ω_c is given by

$$\tau = 2\mu\varepsilon = \mu[\nabla\boldsymbol{u} + (\nabla\boldsymbol{u})^{\mathrm{T}}], \tag{3.2}$$

with μ being the viscosity, ε the strain-rate tensor, and the superscript T representing the transpose of the velocity gradient $\nabla\boldsymbol{u}$. In the drop phase Ω_d the stress is given by the upper convected Maxwell (UCM)
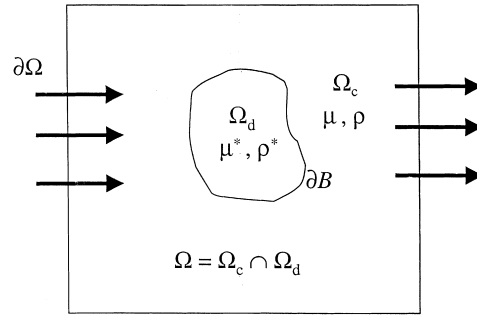
Fig. 3. Flow geometry.

model

$$t_M \hat{\tau} + \tau = 2\mu^* \varepsilon, \tag{3.3}$$

where t_M is the relaxation time, and $\hat{\tau}$ indicates the upper convected (Oldroyd-B) derivative of the stress

$$\hat{\tau} = \frac{\partial \tau}{\partial t} + \boldsymbol{u} \cdot \nabla \tau + \nabla \boldsymbol{u} \cdot \tau + \tau \cdot \nabla^T \boldsymbol{u}. \tag{3.4}$$

The contribution due to the interfacial tension producing the jump in the normal stress across the interface is represented as a (singular) distributed body force. The flow field is incompressible,

$$\nabla \cdot \boldsymbol{u} = 0. \tag{3.5}$$

The velocity field satisfies a single equation in both phases with a spatially-varying density $\rho(\boldsymbol{x})$ that satisfies

$$\frac{D\rho}{Dt} \equiv \frac{\partial \rho}{\partial t} + \boldsymbol{u} \cdot \nabla \rho = 0. \tag{3.6}$$

Other transport properties such as viscosity $\mu(\boldsymbol{x})$ can be similarly handled. Moreover, by applying the momentum equation (3.1) in a pill-box of vanishing thickness straddling the front, one can recover traditional velocity and shear stress continuity across the front, and the jump in the normal stress due to interfacial tension ([42], p. 36).

3.2. Imposed flow fields

Assume that a two-dimensional drop with an initial circular cross section and radius a, is situated at a distance R ($R \gg a$) from the vortex center as shown in Fig. 1. A linearized approximation of the velocity field induced near the drop is

$$\boldsymbol{u}_0^V(\boldsymbol{x}) = \boldsymbol{E}[\boldsymbol{x}_c(t)] \cdot \boldsymbol{x} = \boldsymbol{E}[R\cos\theta(t), R\sin\theta(t)] \cdot \boldsymbol{x} = \dot{\gamma} \begin{pmatrix} \sin 2\theta & -\cos 2\theta \\ -\cos 2\theta & -\sin 2\theta \end{pmatrix} \begin{pmatrix} x \\ y \end{pmatrix}, \tag{3.7}$$

where $\boldsymbol{E}[\boldsymbol{x}_c(t)]$ is the velocity gradient tensor evaluated at the center of the undeformed drop $\boldsymbol{x}_c(t) = \{R\cos\theta(t), R\sin\theta(t)\}$, $\dot{\gamma} = \Gamma/(2\pi R^2)$, Γ being the circulation of the vortex. $\theta(t) = 2\pi t/T = \omega t/2$, denotes the angular position of the center $\boldsymbol{x}_c$, as it revolves around the vortex with circular speed $v_R = \Gamma/(2\pi R)$. The time period of revolution of the drop center $\boldsymbol{x}_c$ is given by $T = 2\pi R/v_R = 4\pi^2 R^2/\Gamma$, and $\omega = 4\pi/T = 2\dot{\gamma}$ is the corresponding circular frequency.

A generalization to a rotating extensional flow $\boldsymbol{u}_0^{\mathrm{RE}}$ is given by the same Eq. (3.7) but with independently varying ω and $\dot{\gamma}$

$$\boldsymbol{u}_0^{\mathrm{RE}}(\boldsymbol{x}) = \dot{\gamma} \begin{pmatrix} \sin \omega t & -\cos \omega t \\ -\cos \omega t & -\sin \omega t \end{pmatrix} \begin{pmatrix} x \\ y \end{pmatrix}. \tag{3.8}$$

OE flow (Fig. 2b) is defined by

$$\boldsymbol{u}_0^{\mathrm{OE}} = -\dot{\gamma} \cos \omega t \begin{pmatrix} 0 & 1 \\ 1 & 0 \end{pmatrix} \begin{pmatrix} x \\ y \end{pmatrix}. \tag{3.9}$$

For $\omega = 0$, both RE and OE flows reduce to steady planar extensional flows.

3.3. Boundary conditions

The interface ∂B is determined by the kinematic condition

$$\frac{\mathrm{d}\boldsymbol{x}_B}{\mathrm{d}t} = \boldsymbol{u}(\boldsymbol{x}_B). \tag{3.10}$$

The delta function $\delta(\boldsymbol{x} - \boldsymbol{x}_B)$ can be used to relate the velocity at a point on the interface $\boldsymbol{u}(\boldsymbol{x}_B)$ to the field velocity.

$$\boldsymbol{u}(\boldsymbol{x}_B) = \int_{\Omega} \mathrm{d}\boldsymbol{x}\, \delta(\boldsymbol{x} - \boldsymbol{x}_B) \boldsymbol{u}(\boldsymbol{x}). \tag{3.11}$$

The velocity field (3.7) or (3.8) provides the external boundary condition at $\partial \Omega$

$$\boldsymbol{u}(\boldsymbol{x} \in \partial \Omega) = \boldsymbol{u}_0(\boldsymbol{x}). \tag{3.12}$$

As noted before, continuity of stress and velocity are automatically satisfied by the governing equation with spatially varying viscosities and the distributed forces (due to interfacial tension) in the field equation.

3.4. Front-tracking preliminaries

Flow with a drop is an example of a multiphase flow in which a suspended phase with properties such as μ^* and ρ^* for viscosity and density are different from those (μ and ρ) in the continuous phase. Furthermore, the two phases are described by different constitutive relations, Newtonian outside and UCM inside the drop. The solution of such problems conventionally involves solving a governing set of equations for each phase, with continuity conditions at the interface. The present method reduces the multiphase to a single phase with spatially varying properties, and thereby eliminates explicit matching at the interface. For this purpose, the material properties are written as

$$\rho(\boldsymbol{x}) = \rho + (\rho^* - \rho)I(\boldsymbol{x}), \tag{3.13}$$

$$\mu(\boldsymbol{x}) = \mu + (\mu^* - \mu)I(\boldsymbol{x}), \tag{3.14}$$

and

$$t_{\mathrm{M}}(\boldsymbol{x}) = t_{\mathrm{M}}I(\boldsymbol{x}), \tag{3.15}$$

where $I(\boldsymbol{x})$ is the indicator function

$$I(\boldsymbol{x}) = \begin{cases} 1, & \boldsymbol{x} \in \Omega_{\mathrm{d}}, \\ 0, & \boldsymbol{x} \in \Omega_{\mathrm{c}}. \end{cases} \tag{3.16}$$

Numerical implementation of Eqs. (3.13)–(3.15) requires smooth representation of the discontinuous indicator function. Applying the gradient operator to Eq. (3.16) we obtain

$$\boldsymbol{G}(\boldsymbol{x}) \equiv \nabla I(\boldsymbol{x}) = \boldsymbol{n}\delta^1(\boldsymbol{n} \cdot (\boldsymbol{x} - \boldsymbol{x}_B)), \tag{3.17}$$

where δ^1 is a one-dimensional delta function. (In a two-dimensional Cartesian coordinate system $\delta(\boldsymbol{x} - \boldsymbol{x}_B) = \delta^1(x - x_B)\delta^1(y - y_B)$.) Using the property of the delta function, we obtain

$$\boldsymbol{G}(\boldsymbol{x}) = \int_{\partial B} \mathrm{d}\boldsymbol{x}_B \boldsymbol{G}(\boldsymbol{x}_B)\delta^1(\boldsymbol{x} - \boldsymbol{x}_B)^{\mathrm{T}}. \tag{3.18}$$

Thus, $\boldsymbol{G}(\boldsymbol{x})$ assumes non-zero values only on the front ∂B. The superscript T represents the direction tangential to the interface. Substituting the definition of $\boldsymbol{G}(\boldsymbol{x}_B)$ from Eq. (3.17), and taking the divergence, we obtain from Eq. (3.18) an equation for $I(\boldsymbol{x})$:

$$\nabla^2 I(\boldsymbol{x}) = \nabla \cdot \boldsymbol{G}(\boldsymbol{x}) = \int_{\partial B} \mathrm{d}\boldsymbol{x}_B \nabla \cdot \boldsymbol{n}\delta(\boldsymbol{x} - \boldsymbol{x}_B), \tag{3.19}$$

with the boundary condition $I(\boldsymbol{x}) = 0$ for $I(\boldsymbol{x} \in \partial\Omega)$, because the interface ∂B, in the present case, is situated far from the domain boundary $\partial\Omega$ and does not straddle it. Note that we have used the separability property of the delta function,

$$\delta(\boldsymbol{x} - \boldsymbol{x}_B) = \delta^1(\boldsymbol{n} \cdot (\boldsymbol{x} - \boldsymbol{x}_B))\delta^1(\boldsymbol{x} - \boldsymbol{x}_B)^{\mathrm{T}}. \tag{3.20}$$

Eq. (3.19) is solved numerically for $I(\boldsymbol{x})$ with a smooth surrogate of the delta function (see Section 4 below). Then Eqs. (3.13)–(3.15) readily furnish the desired 'smooth' fields for the respective properties.

We note that in the front-tracking implementation of Newtonian flows [20,21] with bubbles or free surfaces the gaseous phase could not be ignored, as in other numerical methods. Here the gaseous phase is modeled with small but non-zero values for density and viscosity. Such a treatment arrives at the same set of equations everywhere in the whole domain. A similar approach could have been followed for the difference in constitutive relation between phases, by assuming a Maxwell model also for the continuous phase with a small but finite t_{M}. However, we have implemented the exact condition for a Newtonian fluid, namely $t_{\mathrm{M}} \equiv 0$ in Eqs. (3.2) and (3.15). This requires special treatment for the stress term in the front tracking scheme, as the Maxwell model (3.3) changes character at $t_{\mathrm{M}} = 0$ (see Section 4.2.1).

4. Numerical implementation

For a finite difference implementation the physical domain is approximated by a large box (of size $L_x = L_y = 10.0$ in the unit of the drop radius) which is discretized by a regular square grid. The surface of the immersed drop of radius a ($a/L_{x,y} \ll 1$) is described by line elements. The elements are created by putting points on the circle. The movement of the element vertices describes the evolving shape of the drop. An adaptive regridding scheme prevents the elements from being excessively distorted. The scheme creates/destroys elements by the insertion/removal of points on the existing front.

4.1. Front tracking

A smooth representation of the δ-function, needed for the numerical implementation of Eqs. (3.1), (3.11) and (3.19). We use the procedure of Peskin [43]

$$D(\boldsymbol{x} - \boldsymbol{x}_B) = D^1(x - x_B)D^1(y - y_B), \tag{4.1}$$

where

$$D(x - x_B) = \frac{1}{4\,\Delta x}\left(1 + \cos\frac{\pi}{2\,\Delta x}(x - x_B)\right) \quad \text{for } |x - x_B| \leq 2\,\Delta x. \tag{4.2}$$

The representation is explicitly separable in a Cartesian coordinate system and has the desirable unit measure property (i.e. upon integration over a domain containing $\boldsymbol{x}_B$, it results in unity). The approximation of the delta function is coupled with the discretization of the computational domain; as the discretization length Δx approaches zero, the approximant approaches infinity, as required of a family of regular functions approaching a delta function ([44], p. 110).

Substitution of the above representation of the smoothed delta function and discretization yields the generic integrals:

$$\int_{\Omega} \mathrm{d}\boldsymbol{x}\, f(\boldsymbol{x})\delta(\boldsymbol{x} - \boldsymbol{x}_B) \simeq \sum_i \Delta x\,\Delta y\, f(\boldsymbol{x}_i)D(\boldsymbol{x}_i - \boldsymbol{x}_B), \tag{4.3}$$

where i sums over all grid points in the domain, and

$$\int_{\partial B} \mathrm{d}\boldsymbol{x}_B\, f(\boldsymbol{x})\delta(\boldsymbol{x} - \boldsymbol{x}_B) \simeq \sum_j \Delta l_j\, f(\boldsymbol{x}_j)D(\boldsymbol{x}_j - \boldsymbol{x}_B). \tag{4.4}$$

The index j sums over all front elements, and Δl_j represents the length of the jth element on the front. Expressions similar to Eq. (4.3) are used for Eq. (3.11), and those similar to Eq. (4.4) are used for the interfacial tension term in Eq. (3.1), and in the right-hand side of Eq. (3.19). These representations allow a back-and-forth coupling between the discretized front and the domain variables around it. Thus, we have replaced the interface separating phases by a region with sharp variation in properties. The region has a finite thickness of approximately $4\,\Delta x$ (Fig. 4).

4.2. Finite difference

We have arrived at a system of partial differential equations with smooth spatially varying coefficients. The front has been decoupled from the underlying flow equation, and has been retained only as a means for computing the properties at successive time steps. One may choose from many methods for solving the system of equations in the computational domain. We use a MAC type operator splitting/projection finite difference method. The MAC method solves the system (3.1) and (3.5) in following two explicit steps. The predictor consists of finding an intermediate velocity $\boldsymbol{u}^*$ by

$$\frac{\rho^{n+1}\boldsymbol{u}^* - (\rho\boldsymbol{u})^n}{\Delta t} = -\nabla \cdot (\rho\boldsymbol{u}\boldsymbol{u})^n + F^n + \nabla \cdot \tau^n. \tag{4.5}$$

where F^n is the body force, which includes in the present case the contribution due to the interfacial tension. The density $\rho^{n+1}(\boldsymbol{x})$ is evaluated by Eq. (3.13) from the new front position attained by moving
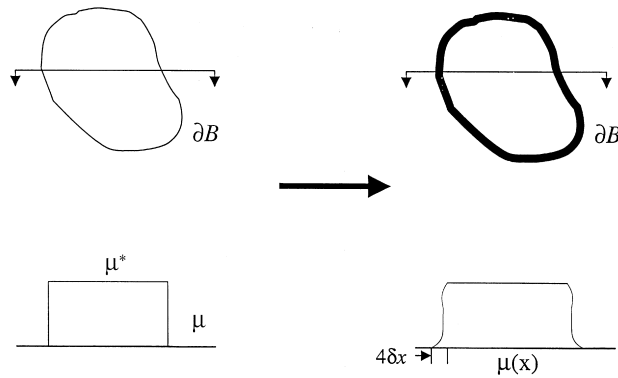
Fig. 4. Front-tracking preliminary.

it explicitly with the velocity u^n. The spatial derivatives are approximated by central differences in their conservative form.

The corrector step gives the final velocity at the next time step u^{n+1},

$$\frac{u^{n+1} - u^*}{\Delta t} = -\frac{1}{\rho^{n+1}} \nabla p^{n+1}. \tag{4.6}$$

Taking the divergence of Eq. (4.6), and requiring that u^{n+1} satisfies continuity, we obtain the following Poisson's equation for the pressure

$$\nabla \cdot \left(\frac{1}{\rho^{n+1}} \nabla p^{n+1} \right) = \frac{1}{\Delta t} \nabla \cdot u^*. \tag{4.7}$$

Details of the method are available in Peyrot and Taylor ([45], p. 160). We use a staggered grid. Boundary values for the nodes just outside the computational domain are obtained by second-order interpolation. A zero Neumann condition for pressure, as is shown to be valid for this explicit method [46], is imposed at the boundary. Note that the final velocity field u^{n+1} is solenoidal, but the intermediate velocity u^* is not.

4.2.1. Constitutive equation

In a naive attempt to integrate the constitutive equations (3.3) and (3.4) following the procedure used for the momentum equation, we obtain

$$\frac{\tau^{n+1} - \tau^n}{\Delta t} = \frac{1}{t_M} \{-\tau + 2\mu\varepsilon - t_M(u \cdot \nabla\tau + \nabla u \cdot \tau + \tau \cdot \nabla^T u)\}^n. \tag{4.8}$$

Note that the present scheme diverges at $t_M = 0$ in the Newtonian phase. The Maxwell equations (3.3) and (3.4) is singular in the limit of $t_M = 0$, as the highest time derivative drops out of the equation. On the other hand, front-tracking implementation demands that we solve the same equation in the whole domain with the relaxation time t_M varying smoothly from its non-zero value inside the drop to zero outside. To arrive at a consistent scheme we write Eq. (3.3) in the following form:

$$t_M \frac{\partial \tau}{\partial t} + \tau = K(t), \tag{4.9}$$

where

$$K(t) = 2\mu\varepsilon - t_M(\boldsymbol{u} \cdot \nabla\tau + \nabla\boldsymbol{u} \cdot \tau + \tau \cdot \nabla^T\boldsymbol{u}). \tag{4.10}$$

The equation (4.9) can be integrated by parts to arrive at the following exact expression

$$\tau(t_n + \Delta t) - \tau(t_n)e^{-\Delta t/t_M} = K(t_n + \Delta t) + K(t_n)e^{-\Delta t/t_M} - \int_{t_n}^{t_n+\Delta t} e^{-t/t_M}\frac{\partial K}{\partial t}\, dt. \tag{4.11}$$

Neglecting the integral, i.e. assuming $K(t_n + \Delta t) \simeq K(t_n)$, we obtain the difference scheme

$$\tau^{n+1} = \tau^n e^{-\Delta t/t_M} + K^n(1 - e^{-\Delta t/t_M}). \tag{4.12}$$

The above difference scheme is consistent everywhere (including where $t_M = 0$); the exponential time variation has been retained explicitly. In passing we note that the above procedure can be applied to a large class of differential constitutive relations that have the form (4.9) with the desired result. We also note that we could arrive at an implicit or semi-implicit scheme by choosing K^{n+1} or $(K^n + K^{n+1})/2$ in the right-hand side of Eq. (4.12). Furthermore making the approximation $e^{-\Delta t/t_M} \simeq 1 - \Delta t/t_M + O(\Delta t/t_M)^2$, we obtain

$$\tau^{n+1} - \tau^n = \frac{\Delta t}{t_M}(K^n - \tau^n), \tag{4.13}$$

which is identical to the original scheme (4.8).

Another consequence of this approach is a natural splitting of the elastic and the viscous stresses. Given Eq. (4.10), one can write Eq. (4.12) as

$$\tau^{n+1} = \tau^n e^{-\Delta t/t_M} + 2\mu\varepsilon^n - 2\mu\varepsilon^n e^{-\Delta t/t_M} + t_M(\boldsymbol{u} \cdot \nabla\tau + \nabla\boldsymbol{u} \cdot \tau + \tau \cdot \nabla^T\boldsymbol{u})^n(1 - e^{-\Delta t/t_M}). \tag{4.14}$$

Using $2\mu\varepsilon^{n+1}$ instead of $2\mu\varepsilon^n$ in the second term we can express it as

$$\tau^{n+1} = \tau_N^{n+1} + \tau_P^{n+1}, \quad \tau_N = 2\mu\varepsilon \tag{4.15}$$

is the Newtonian part, and the polymeric part τ_P is given by

$$\tau_P^{n+1} = (\tau^n - 2\mu\varepsilon^n)e^{-\Delta t/t_M} + t_M(\boldsymbol{u} \cdot \nabla\tau + \nabla\boldsymbol{u} \cdot \tau + \tau \cdot \nabla^T\boldsymbol{u})^n(1 - e^{-\Delta t/t_M}). \tag{4.16}$$

Note that $t_M \to 0$ gives $\tau_P \to 0$. Elastic viscous stress splitting, originally proposed by Perera and Walters [47], has been executed in most numerical schemes (see, e.g. [26,28,29]). It allows preserving the elliptic nature of the problem and thus enhances stability. In fact Sun et al. [28] proposed an adaptive splitting (AVSS) where the Newtonian part is chosen with a varying artificial solvent viscosity that would make the elliptic term suitably dominant, and thereby ensure stability. However, in absence of a solvent viscosity as is the case in UCM (in contrast to Oldroyd-B) the splitting becomes cumbersome, involving the upper convected derivative of the strain rate tensor. In the above scheme the splitting is natural and does not involve differentiation of strain rates.

Even in finite difference schemes inclusion of a diffusion operator lends robustness to the iteration algorithm. Oliveira et al. [36] added a numerical diffusion term in both sides of the momentum equation

and treated one as an explicit inactive source and the other as an active elliptic operator, the latter giving rise to the algebraic coefficients that regulate convergence of the iterative algorithm. A similar self-consistent false diffusion scheme for constitutive equations was used by Huang et al. [48] to make the iteration stable. It may also be pertinent here to note the recent computation of viscoelastic drops by Toose et al. [41]. He applied a boundary element method based on Stokes Green's function for an Oldroyd-B fluid. The Stokes operator is readily available due to the solvent viscosity term; the non-Newtonian part is treated as a source term using finite element discretization inside the drop. Finite volume implementation of [37] for an unsteady finite Reynolds number simulation through planar contraction uses a similar explicit MAC scheme for a single phase flow again for an Oldroyd-B model. All of these attempts demonstrate the importance of an explicit diffusion operator in the momentum equation, which has been naturally incorporated in the above analytical integration technique not only for UCM, but for a class of differential constitutive equations.

The stress terms are discretized on the staggered grid with τ_{xx} and τ_{yy} being represented at the pressure nodes that are at the center of an element (with velocity at the element face), and τ_{xy} at the vertices of the elements. This choice has been made to provide proper coupling between the velocity and their driving stresses as for the pressure term in a Newtonian case. The convective terms in Eq. (4.14) are discretized with first order upwinding, i.e. while interpolating stress at the velocity node, the value from the upstream side is used, neglecting the downstream influence. A second-order accurate QUICK scheme was also implemented after the traditional central differencing failed for high Weissenberg number without any alleviation of the convergence difficulties.

We should mention that no additional boundary conditions on the stresses are required, unlike single-phase viscoelastic computation, because at the boundary the fluid is Newtonian, and all of the elastic stress terms vanish.

4.2.2. ADI for viscous terms

It is well known from the Newtonian literature that the above explicit scheme suffers from dual restrictions on time steps, viz. from diffusion at low Reynolds number ($\Delta t < 0.25(\Delta x)^2/\nu$) (note that Mompean and Deville [37] used only the solvent viscosity, which in our case is equal to zero inside the drop, to define the stability limit equation (24) of their paper) and from advection at high Reynolds number ($\Delta t < 2.0\nu/U_{\max}^2$) ([45], p. 148). For our particular applications relevant to emulsions, the low Reynolds number constraint is important. As mentioned earlier, the available literature on emulsions is largely restricted to zero Reynolds number, and we wish to compare our results with these. To relieve the low Reynolds number restriction on time step, we split the predictor step further, and treat the diffusive terms by ADI. A similar treatment was first successfully executed by Goda [49] for cavity flows. Eq. (4.5) for this step is split into three parts,

$$\frac{\rho^{n+1}\boldsymbol{u}^{***} - (\rho\boldsymbol{u})^n}{\Delta t} = -\nabla \cdot (\rho\boldsymbol{uu})^n + F^n + \nabla \cdot \tau_{\mathrm{P}}^n + D_{xy}(\boldsymbol{u}^n), \tag{4.17}$$

$$\rho^{n+1}\left(\frac{\boldsymbol{u}^{**} - \boldsymbol{u}^{***}}{\Delta t}\right) = D_{yy}(\boldsymbol{u}^{**}), \tag{4.18}$$

$$\rho^{n+1}\left(\frac{\boldsymbol{u}^* - \boldsymbol{u}^{**}}{\Delta t}\right) = D_{xx}(\boldsymbol{u}^*). \tag{4.19}$$

The viscous term in Eq. (4.5) is also expressed in three parts,

$$\nabla \cdot \tau_N = D_{xy} + D_{yy} + D_{xx}, \tag{4.20}$$

where D_{xx} and D_{yy} are terms involving double derivatives with respect to either x or y, and D_{xy} are the mixed derivatives. Mixed derivatives are treated along with advection in an explicit manner, as in Eq. (4.17), while the terms involving double derivatives are handled implicitly along alternating directions, first y (Eq. (4.18)), and then x (Eq. (4.19)). Each of these implicit equations gives rise to a tri-diagonal system that is solved by Thom's algorithm. However, while an explicit scheme does not require boundary values for the intermediate variables (those marked with *), they must be prescribed in an implicit method. We use

$$\boldsymbol{u}^* = \boldsymbol{u}^{**} = \boldsymbol{u}^{***} = \boldsymbol{u}^{n+1}, \quad \text{at } \partial\Omega, \tag{4.21}$$

and consequently the zero Neumann condition on the pressure is retained. Early theoretical studies by Temam indicated that imposing final step values on the intermediate variables at the boundary is a sufficient condition for convergence as $\Delta x, \Delta t \to 0$ ([45], p. 165). There have been several attempts to improve the order of the method by employing smart conditions for the intermediate velocities and the pressure [50,51]. However, Perot [52] has shown that the present prescription is consistent with an LU decomposition of the original operator.

Although ADI formally removes the restriction on time steps, it is well known that in practice care is required when implementing such a fractional step algorithm. We also adhere to a Courant–Frederichs–Lewy (CFL) criterion $\Delta t < \Delta x / U_{\max}$. Furthermore, the maximum norm of the velocity field is monitored for any unsatisfactory behavior, and the time step is halved when warranted. An explicit Euler integration scheme was used for time marching. A multigrid method ([53], p. 106) was applied for the solution of Poisson's equations for the pressure (4.7) and the indicator function (3.19).

4.3. Algorithm

Here we mention the steps of our algorithm. Given a discretized drop shape, we solve Eq. (3.19) with the smoothed right-hand side of Eq. (4.3) to obtain a representation of the indicator function, and thereby find the spatially varying material properties (3.13)–(3.15). The solution is obtained in a regular 2D grid using a multigrid Poisson solver. Then we solve the single-phase boundary value problem (with smoothly varying density, viscosity and relaxation time) with the above described ADI finite difference scheme in the 2D grid to obtain the velocity at the grid points. The smoothed representation (4.4) is used for the force due to the interfacial tension in Eq. (3.1). The velocity at the grid point is used to interpolate the velocity at the front points by Eq. (3.11), again using Eq. (4.3) for the delta function. The new interface is found by moving it with the front velocity (3.10). The front is regridded, comparing the element length to Δx by insertion/removal of points.

5. Numerical results

The problem is non-dimensionalized, using drop radius a and $\dot{\gamma}^{-1}$ as the length and the time scales, respectively. For the steady problem there are five non-dimensional parameters: Reynolds number, $Re = \rho\dot{\gamma}a^2/\mu$, $k = Ca^{-1} = \sigma/(\dot{\gamma}\mu a)$ (inverse capillary number), $\lambda = \mu^*/\mu$, $\lambda_\rho = \rho^*/\rho$ and the

Weissenberg number, $Wi = t_M \dot{\gamma}$. For the case of a vortex, the non-dimensional frequency (Strouhal number) $St = \omega/\dot{\gamma} = 2$. However, for general rotating extensional flows it assumes arbitrary values. Since we have not considered gravity effects in our simulation, λ_ρ appears in the problem only through the drop Reynolds number, $Re^* = Re\,\lambda_\rho/\lambda$. For brevity, we restrict results to the case of $\lambda_\rho = 1.0$, $\lambda = 1.0$. In a typical experiment with an alcohol (immiscible in water) drop ($\mu^* = 0.018\,\mathrm{g\,cm^{-1}\,s^{-1}}$, $\rho^* = 0.82\,\mathrm{g\,cm^{-3}}$) of radius $a = 1\,\mathrm{cm}$ suspended in water ($\mu = 0.01\,\mathrm{g\,cm^{-1}\,s^{-1}}$, $\rho = 1.0\,\mathrm{g\,cm^{-3}}$), the interfacial tension is of the order 1–$10\,\mathrm{dyn\,cm^{-1}}$. Therefore, with $\dot{\gamma} = 0.1\,\mathrm{s^{-1}}$ one obtains $Re = 10$, $\lambda = 1.8$, $\lambda_\rho = 0.82$ and k, 1000–$10{,}000$ ([54], p. 17). We performed a grid convergence study, and found that 81×81 grid points, did not show significant changes in drop shape from 129×129, and therefore an 81×81 grid is believed sufficient for our purpose. Similarly the effect of domain size has also been investigated by increasing it to twice the present size ($L_x = L_y = 10.0$) with no significant change in results. Note that Taylor [3,4] suggested a deformation criterion $D = (L - l)/(L + l)$, (where L (l) is the maximum (minimum) distance of the drop surface from the center), that is based on the observation that the drop assumes an approximately elliptical shape in steady shear and extensional flows. Although the same criterion has been adopted here, we have found that for an arbitrary deformation D, the results can be misleading. Two nearly identical shapes may result in significantly different values of D. This is because D is computed with the information about only two surface points, and therefore is extremely sensitive to the numerical description of the surface. Our method, based on an interface smoothed over $4\,\Delta x$, is inherently approximate for the exact location of the interface. The choice of an 81×81 grid (16 grid points across the drop diameter) is based on an ability to describe the shape rather than D. From our convergence study and the satisfactory match with analytical results [2], we believe that the values of D computed below depict correct trends.

5.1. Vortex

The literature on emulsions is largely restricted to steady Stokes flow. Our code is limited to low but finite Reynolds number. As a low Reynolds number case, we choose $Re = 0.1$. In [1] we have investigated the effects of varying interfacial tension and observed that a sufficiently high value of interfacial tension (i.e. large k) is able to inhibit the growth, keeping the deformation bounded. Moreover, D was seen to reach a constant value in the large time limit, as though the drop assumes an elliptic shape and goes on rotating in response to the rotating stretching field. However, the drop does not undergo rigid rotation; its principal axes of deformation rotate. Fig. 5 shows the evolution of $D = (L - l)/(L + l)$ (where L (l) is the maximum (minimum) distance of the drop surface from the center) with time at $k = 7.599$. The evolution of D for a particular value of Wi shows behavior similar to that of the viscous case [1]. With increasing Weissenberg number the long-time deformation decreases progressively from its Newtonian value until $Wi \simeq 0.628$. However, for $Wi = 6.283$ the drop displays oscillation with the average value of the deformation showing an increase from $Wi = 0.628$. The long-time values of D have been plotted in the inset where the non-monotonic behavior is clearly visible. Note that this behavior is different from that observed in the viscous case [1,2], where with variation of different parameters of the flow the deformation displayed a 'resonance' peak. To explain the behavior, we have offered a simple ODE model for the problem in the Appendix A, with a linear Maxwell relation. Note that the model is only a representative one, and is not expected to quantitatively match the solution. However, it serves to explain the trends of the solution, as well as to emphasize the fact that a viscoelastic constitutive relation is indeed capable of the complex behavior observed in the numerical solution. The long-time periodic response
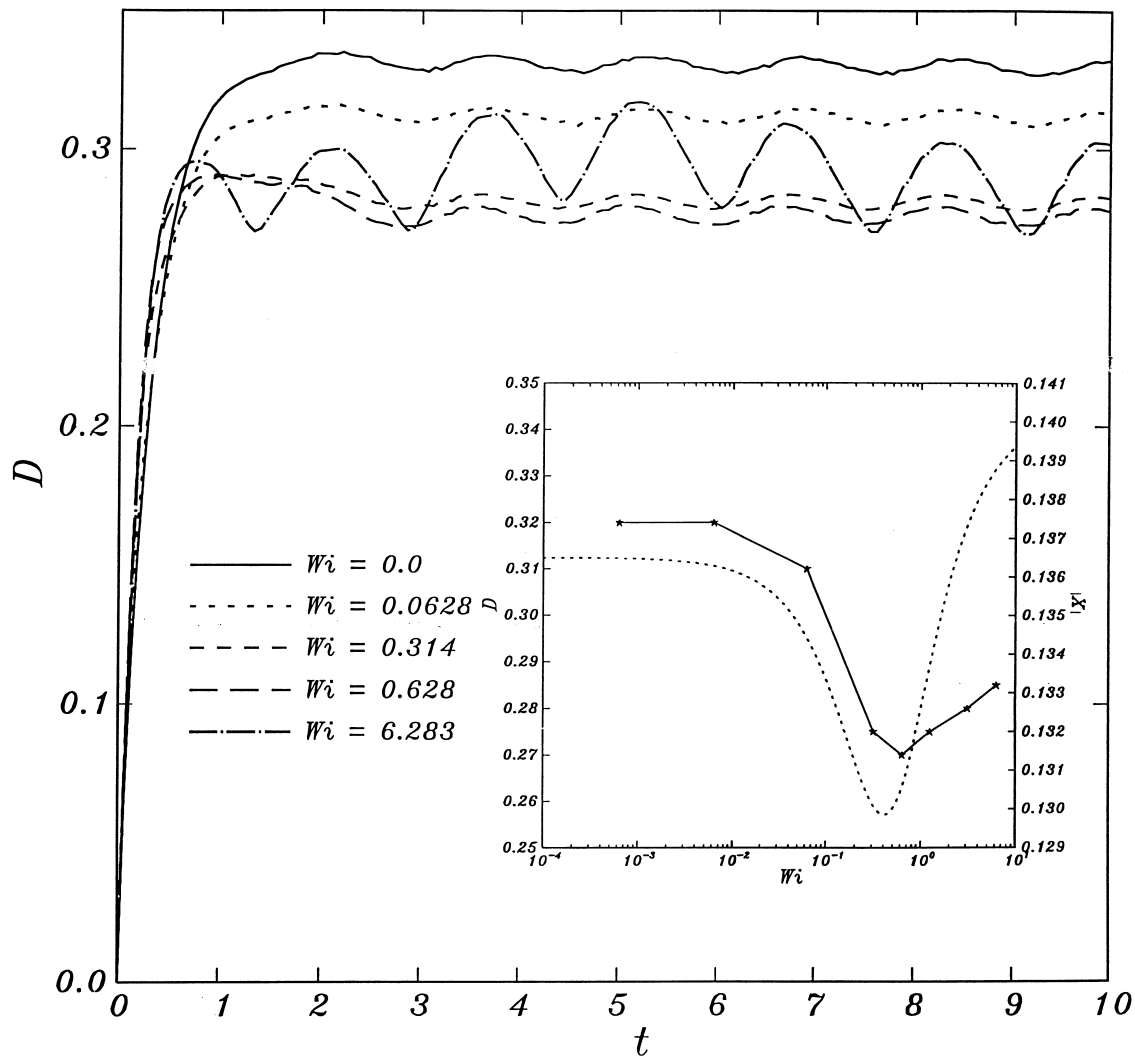
Fig. 5. Effect of relaxation time on drop deformation in a potential vortex; $Re = 0.1$, $k = 7.599$. In the inset long-time D (solid line) is plotted with varying relaxation time. On the right ordinate the ODE model response, i.e. modulus of Eq. (A.5) is plotted (dotted line). Note that the range of values are different in right- and left-axes.

(A.5) from the model plotted at the right ordinate axis of the same plot shows similar non-monotonic behavior. As explained in the Appendix A, the immediate decrease in response with viscoelasticity is due to the increased spring constant inhibiting the deformation. However, for large enough Wi, the contribution due to elasticity decreases to zero, and the effect of decreasing damping leads to increased response. In Fig. 6, we show the long-time revolution of the drop, maintaining the elliptic shape for a specific case of $Wi = 0.6283$ at different instants of time over a period of the vortex. The first and the last drop traces, that are roughly one period away ($\Delta t = 6.35$, while $T = 2\pi$), are almost identical.

In Fig. 7, we present the evolution of D with time for an intermediate Reynolds number $Re = 1.0$, and at $k = 12.66$. The figure here is very similar to the one for $Re = 0.1$ marked by decreasing D
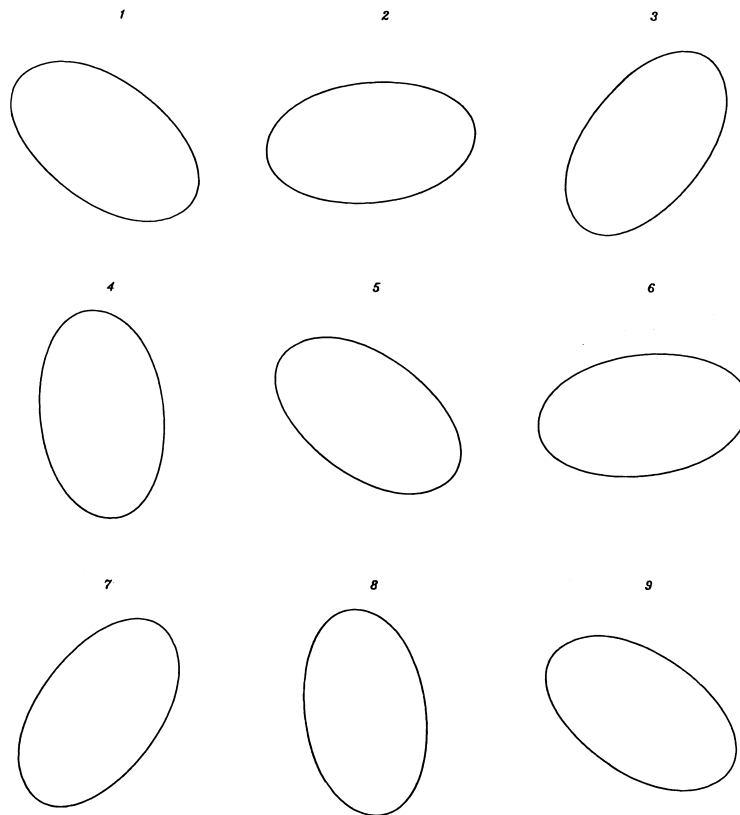
Fig. 6. Drop shapes in a potential vortex at $t = 38.01$, 38.77, 39.59, 40.36, 41.18, 41.94, 42.77, 43.53, and 44.35 (from top left to bottom right), over a period; $Re = 0.1$, $k = 8.0$, $t_M = 6.283$.

with increasing Wi and pronounced oscillation for high Wi curves. High values of Wi lead to increased non-linearity in the constitutive equation, leading to the oscillations. In the inset, long-time D is plotted as a function of Wi along with the analogous expression from the ODE model. However, for the range of relaxation time investigated, the computed D does not show any increase, in contrast to the model solution. We speculate that the reason for continual decrease is due to the energy expended in shear waves inside the drop due to viscoelasticity. In Appendix B, we have described the physics underlying the wave phenomenon. Note that from Eq. (B.3) l_w/a becomes O(1) for $Wi \sim 10$ for this Reynolds number. It is noted in the viscous computation [1] that higher inertia leads to an overshoot in D before one reaches the long-time limit, an effect of the finite Reynolds number of the simulation. The initial overshoot is more prominent in Fig. 8 for $Re = 10.0$ and $k = 38$. For this case we experienced convergence difficulty for simulations at high Weissenberg numbers. The long-time D shows a decrease with Wi in the inset. The ODE response is entirely different, indicating failure of the model to describe the physics at high Re. However, it is interesting to note that for this case the ODE response does not show a decrease from the viscous case, for the inertia term dominates the spring term as explained in the Appendix A. In summary, the drop settles down as in the viscous case to a steady rotating 'elliptical' shape with a long-time value of D decreasing at least initially with increasing Wi and concurrently showing more oscillations.
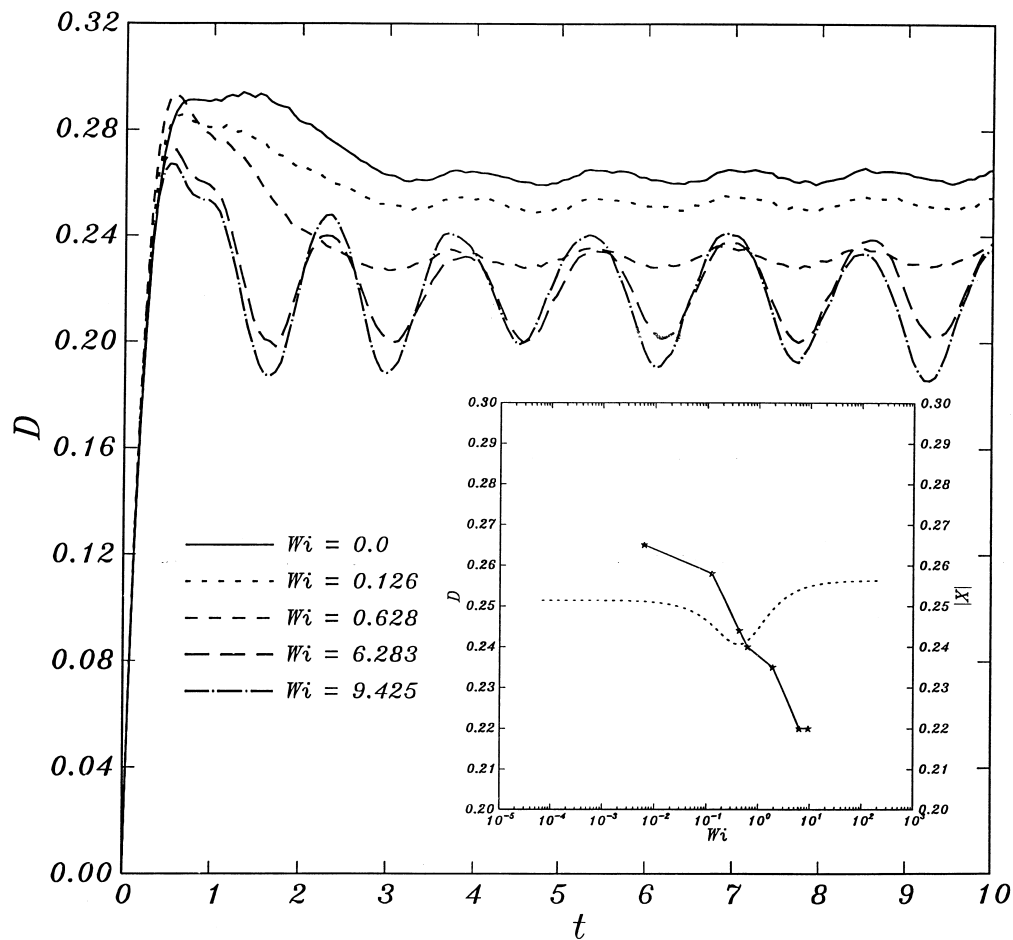
Fig. 7. Effect of relaxation time on drop deformation in a potential vortex; $Re = 1.0$, $k = 12.66$. In the inset long-time D (solid line) is plotted with varying relaxation time. On the right ordinate the ODE model response (dotted line) is plotted.

5.2. Rotating extensional flow

For the vortex flow given by Eq. (3.7), Strouhal number, $St = 2$. By varying St one obtains a rotating extensional flow. One could imagine a circular bath filled with a ferromagnetic fluid to which opposite magnetic fields are applied along a line through the center (i.e. putting magnets of the same polarity at opposite sides of the bath). This could cause a flow where the fluid would be rotating in four cells, due to mass conservation. Along two orthogonal axes of the bath, flow would be towards and away from the center, creating a saddle point in the middle. A drop of a second, ordinary fluid suspended at the center is, therefore, in an extensional flow with shear rate $\dot{\gamma}$, determined by the strength of the applied magnetic fields. On rotating the magnetic field around the bath with a frequency ω, the desired rotating extensional flow is obtained in the vicinity of the drop. We have investigated such a general rotating extensional flow (3.8) in detail for a Newtonian drop in [1], varying the Reynolds number, frequency and the interfacial tension, and observed a resonance phenomenon where the deformation behaves non-monotonically with parameters.
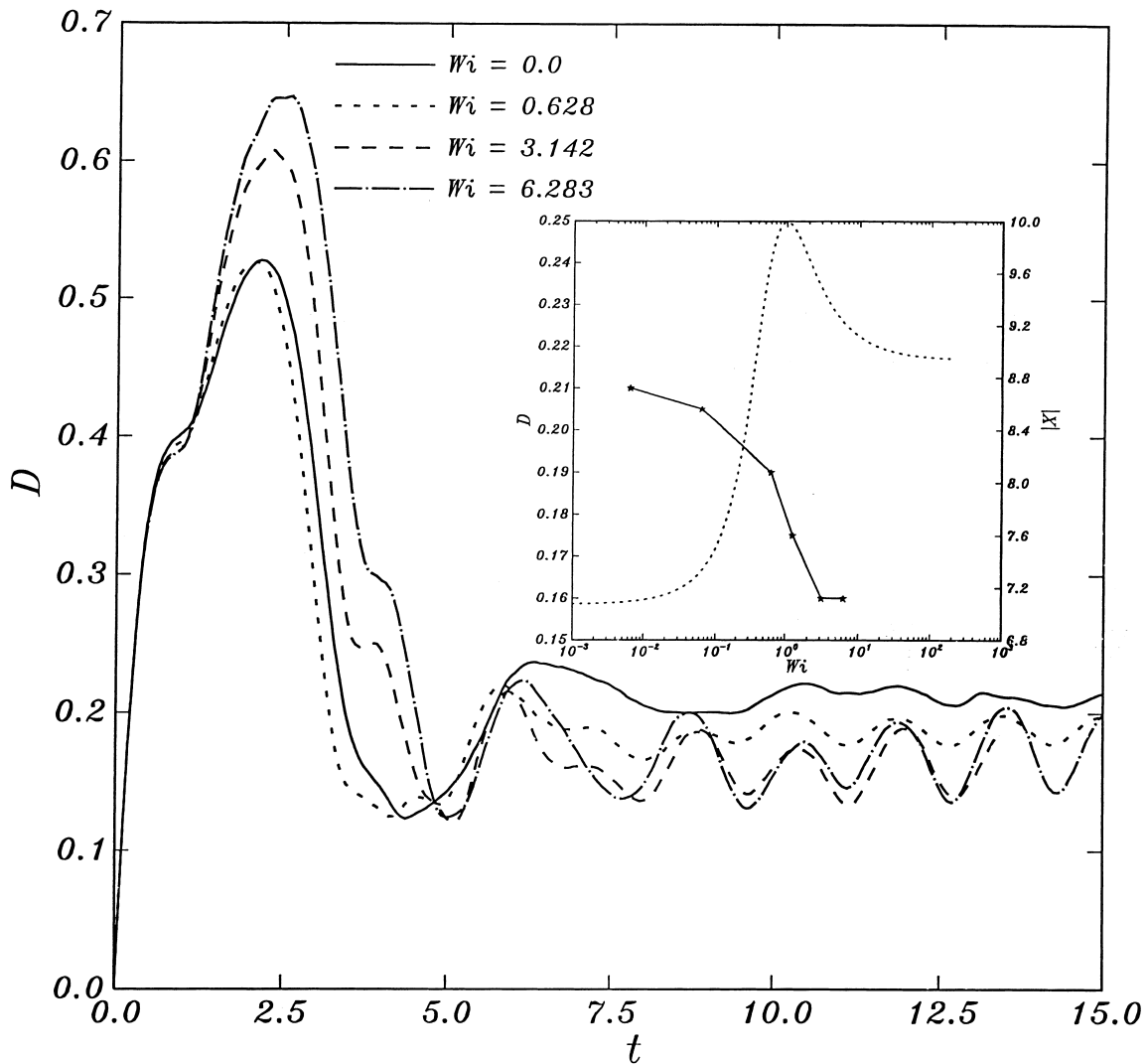
Fig. 8. Effect of relaxation time on drop deformation in a potential vortex; $Re = 10.0$, $k = 38.0$. In the inset long-time D (solid line) is plotted with varying relaxation time. On the right ordinate the ODE model response (dotted line) is plotted. Note that the range of values are different in right- and left-axes.

Here we study the deformation in an RE flow (3.8) restricting ourselves to $Re = 0.1$ and 1.0, and study the effects of Wi variation. For $Re = 0.1$, we first consider a steady extensional flow, i.e. $St = 0.0$. In Fig. 9, the drop deformation D is plotted as a function of time for varying Weissenberg number at $k = 8$. The growth in deformation is initially steeper than Newtonian, the effect growing with Wi, but later they cross, and the long-time D is smaller for a more viscoelastic drop. Similar results were observed by Toose et al. [41], in their inertialess study of an Oldroyd-B drop. They offered an explanation by the presence of two time-constants in the process, and successfully modeled it using simple exponential functions.
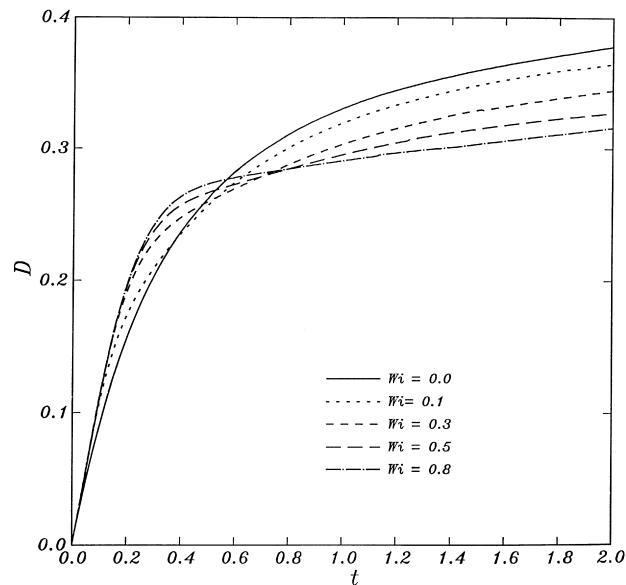
Fig. 9. Effect of relaxation time on drop deformation in a steady extensional (RE with $St = 0.0$) flow; $Re = 0.1, k = 8.0$.

To study the effects of rotation of the stretching axis for a general rotating flow we choose $St = 4\pi$ and $k = 8$ at $Re = 0.1$ (i.e. the same case for the steady flow in Fig. 9), dynamics of the case having been described in detail for a Newtonian drop in [1,2]. In Fig. 10, as before, D is plotted as a function of time for varying Wi. We observe that the long-time D plotted in the inset along with the ODE response increases from the Newtonian case until $Wi \simeq 0.5$ and then decreases. Note that compared to the vortex case (Fig. 5), for which all parameters but St are the same (k for the vortex was 7.599, sufficiently close to the present value of 8), D displays entirely different behavior. The response from the ODE model shows similar behavior. As mentioned in the Appendix A, depending on which of the two terms (spring constant and inertia) dominates the dynamics, effects of adding viscoelasticity can be different. In this case of large St (i.e. inertia dominated), apart from increased damping, added elasticity works against inertia, and therefore leads to an increased D initially. For $Re = 1.0$ we plot evolution of D for $k = 50$ and $St = 4\pi$ in Fig. 11. Here the behavior is dissimilar to what has been seen before in that D increases with increasing Wi, as is evident from the long-time limit shown in the inset. Here too the effects of a shear wave are important because of higher Re and the results deviate from the ODE response. Note that from Eq. (B.3) $l_w/a = 1$ for $Wi = 0.25$, close to the value where the numerical D curve increases from a temporary plateau.

5.3. Oscillating extensional flow

An oscillating extensional (OE) flow (3.9) can be generated by a four-roll mill [12] by varying the rotation rate of the rolls in a time-periodic way. Here we briefly present computational results for such a flow for the same parameter values as those adopted for the RE flow. For an OE flow where the stretching and the contraction take place alternately along two orthogonal axes, the drop likewise alternates its axes of extension and contraction [1,2]. In Fig. 12a D is plotted for $Re = 0.1, k = 8$ and $St = 4\pi$, and
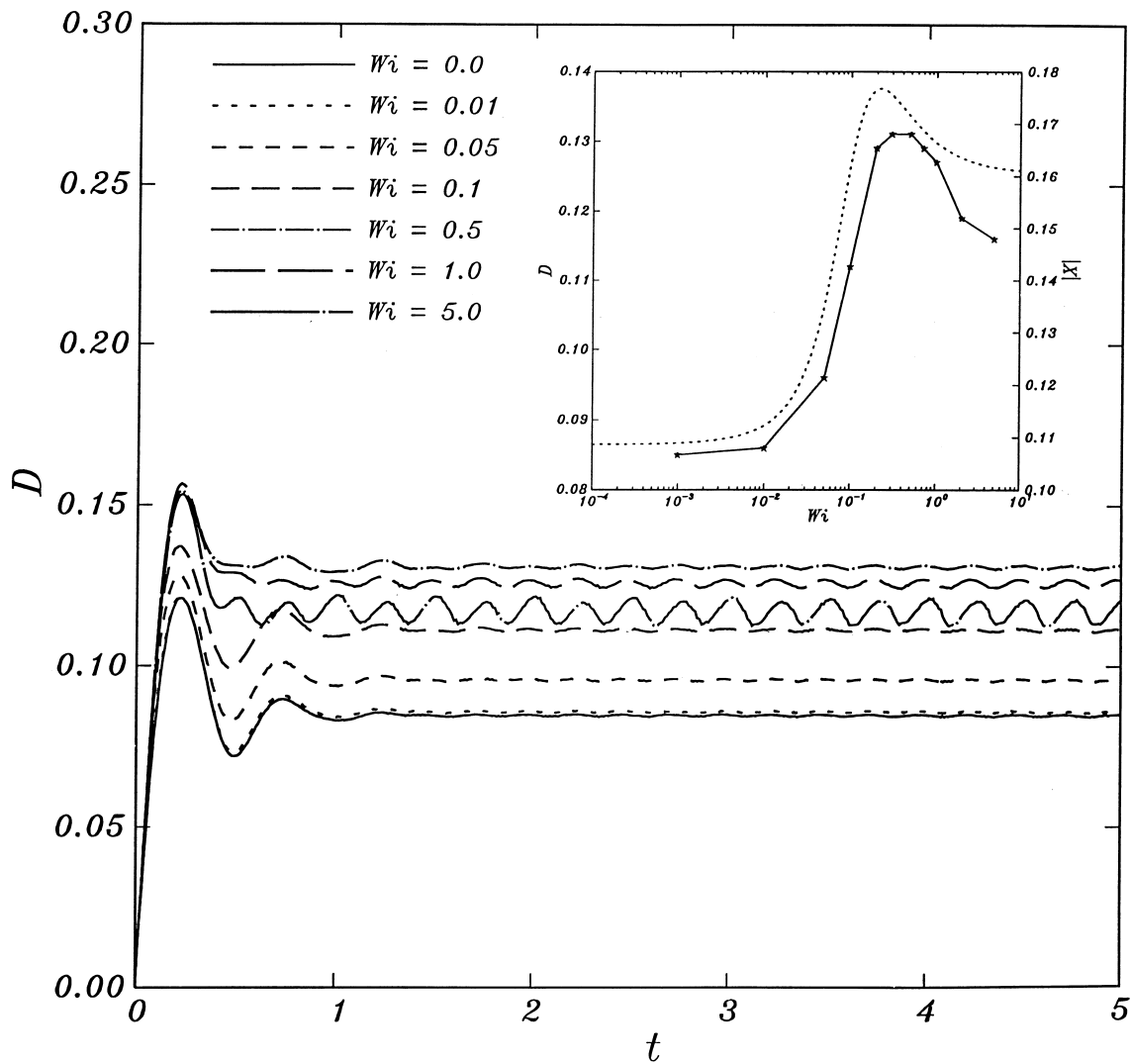
Fig. 10. Effect of relaxation time on drop deformation in an RE flow; $Re = 0.1$, $k = 8.0$, $St = 4\pi$. In the inset long-time D (solid line) is plotted with varying relaxation time. On the right ordinate the ODE model response (dotted line) is plotted. Note that the range of values are different in right- and left-axes.

it oscillates from a maximum value to zero as in the viscous case. The effect of Wi is shown for two successive periods ($St = 4\pi$ gives $T = 0.5$), after the initial transients have died away. The maximum values of D are seen to vary non-monotonically with Wi. The traces of the drop shapes are plotted in Fig. 12b to depict the oscillatory behavior over a period. The drop is seen to change its axes of contraction and extension. The perturbative analysis in [2], however, showed (and the numerical results agreed with it) that the maximum D would be close to that of the RE flow in the long-time limit. For comparison $D_{\max}$ for $Re = 0.1$ and 1.0 are plotted along with their counterpart (D) from rotating extensional flow
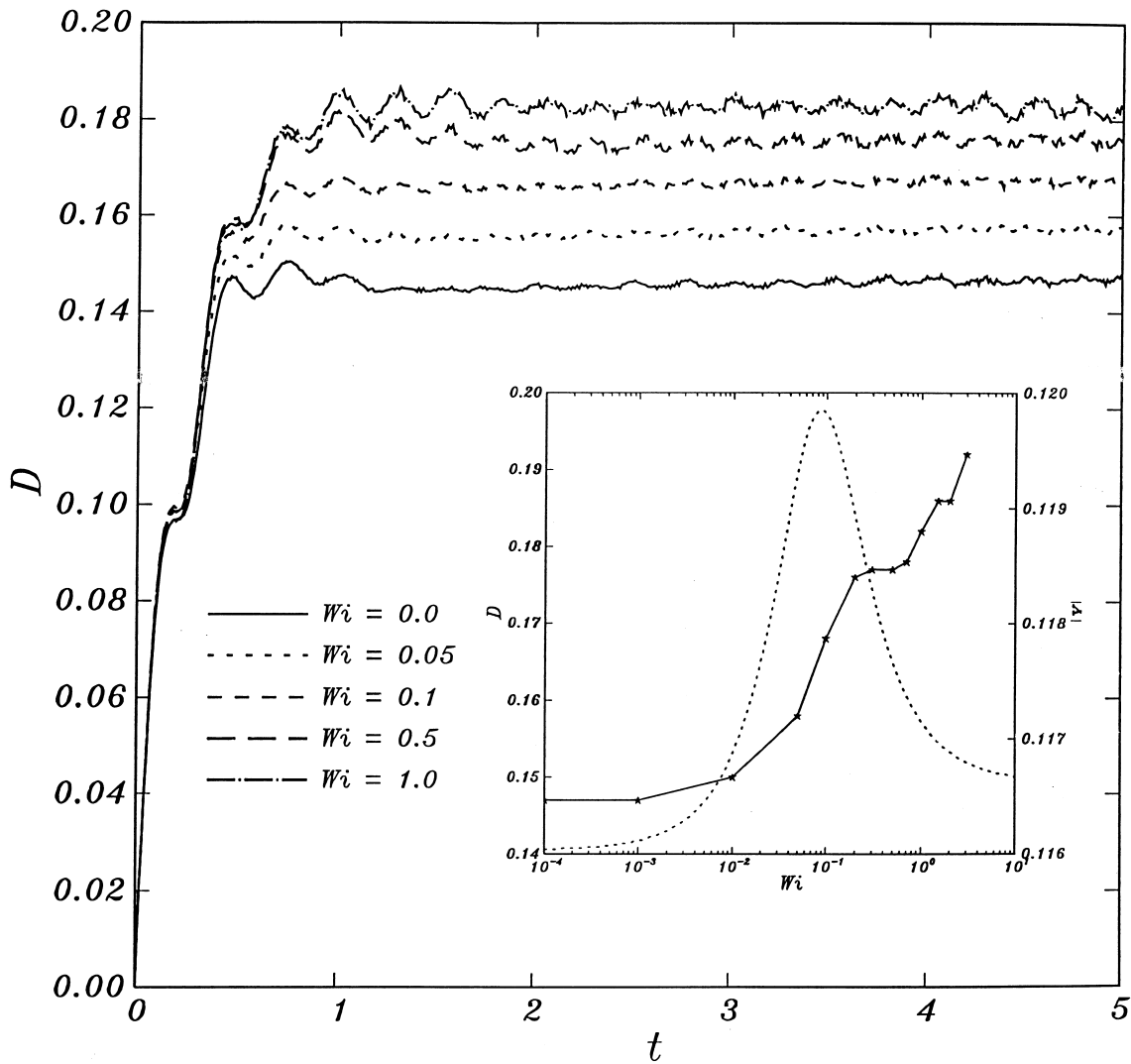
Fig. 11. Effect of relaxation time on drop deformation in an RE flow; $Re = 1.0$, $k = 50.0$, $St = 4\pi$. In the inset long-time D (solid line) is plotted with varying relaxation time. On the right ordinate the ODE model response (dotted line) is plotted. Note that the range of values are different in right- and left-axes.

(Figs. 10 and 11) in Fig. 13. The curves for $Re = 0.1$ are closer than for $Re = 1.0$. However, in both cases RE and OE flows show remarkable similarity despite their dissimilar nature.

6. Discussion and summary

We have numerically simulated the deformation of a two-dimensional viscoelastic drop suspended in a Newtonian fluid. The deformation is produced by a flow due to a potential vortex, its generalization that we
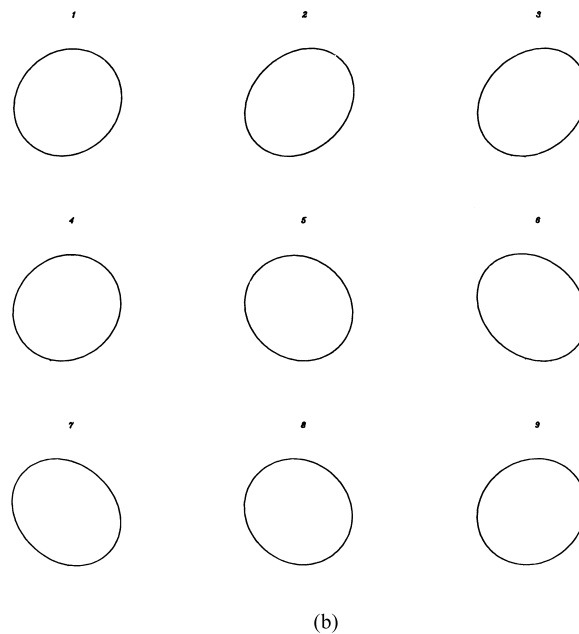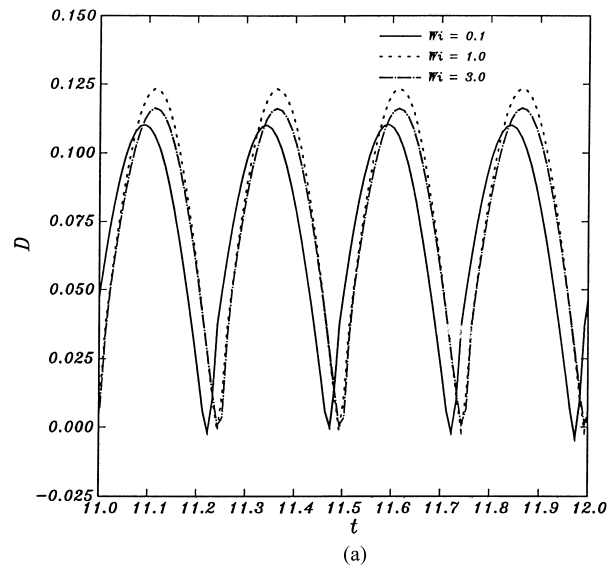
Fig. 12. (a) Effect of relaxation time on drop deformation in an OE flow; $Re = 0.1$, $k = 8.0$, $St = 4\pi$; (b) drop shapes in a potential vortex at $t = 11.253, 11.313, 11.373, 11.433, 11.503, 11.563, 11.623, 11.683$ and 11.753 (from top left to bottom right), over a period; $Re = 0.1$, $k = 8.0$, $t_M = 0.1$.

call rotating extensional flow, and an oscillatory extensional flow at small but non-zero Reynolds numbers. An ADI front-tracking method is used. Viscoelasticity is modeled by the UCM relation. An analytical elastic viscous stress splitting has been developed and implemented to treat the non-Newtonian constitutive equation. Such a treatment can profitably be adopted in a class of differential constitutive equations.
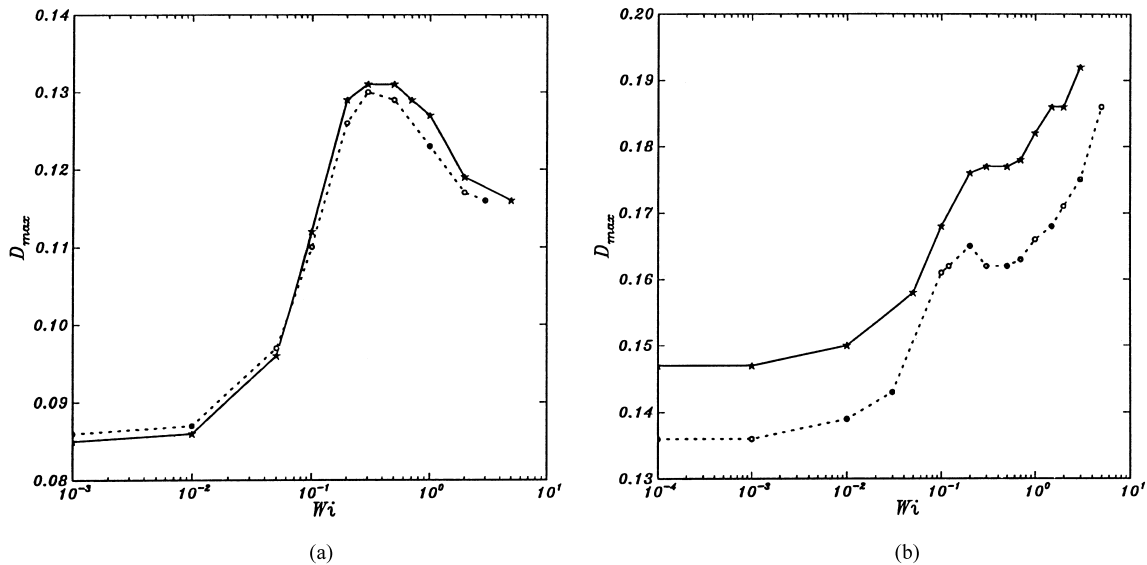
Fig. 13. Long-time drop response with varying relaxation time in an RE (solid line) and an OE (dotted line) flow; (a) Re=0.1, $k = 8.0$, $St = 4\pi$; (b) $Re = 1.0$, $k = 50.0$, $St = 4\pi$.

As in [1], the velocity field due to the vortex has been modeled in the vicinity of the drop by a linear flow with time periodic variation. The linearization introduces an error that is of higher order than a/R, its limitation being discussed in [1].

For the vortex, similar to the viscous case the drop was found to reach a steady value of deformation, indicating a roughly elliptic shape revolving in response to the rotating stretching flow. Finite inertia leads to an overshoot in deformation during the initial transient behavior. With higher Reynolds number the deformation increases, and displays longer and more pronounced transients.

We also investigated drop deformation in a rotating extensional (RE) flow, a generalization of the vortex induced flow with the frequency of rotation varying independently of the shear rate. Therefore, the behavior is similar to that in a vortex, in that the drop reaches a steady value of deformation in the long-time limit. In the zero frequency limit, i.e. for a steady extension, it is found that higher elasticity gives rise to a steeper dynamics initially followed by lower final deformation value, in agreement with [41].

As expected, a non-zero relaxation time adds complexity to the results for a Newtonian drop. In the case of a viscous drop variation of frequency and interfacial tension introduced a resonance behavior, where the drop deformation showed a marked increase near the parameter values where the natural frequency matched the forcing frequency [1,2]. In fact, there we found that variation of density ratio, viscosity ratio and Reynolds number all lead to a characteristic resonance response, albeit with different detail. The resonance is due to the finite Reynolds number of the computation resulting in a 'mass' of the system. The system behaves like a forced, damped oscillator, with the flow playing the role of the forcing at a particular frequency, viscosity the damping and the interfacial tension the spring. The observation inspired a simple ODE model briefly described in Appendix A.

For the present case the variation in relaxation time led to increase and/or decrease in response depending on other parameters, viz. Re, St and k. In search of an explanation, a linear Maxwell relation was introduced

in the ODE model of Appendix A. Its response has explained many of the computed trends. The complexity of the behavior is due to the fact that the Maxwell relation introduces both a damping and an elastic effect, and the resulting response, therefore, is manifestation of a competition between the two.

In a Maxwell model, keeping all other parameters fixed and increasing relaxation time decreases the rigidity as $t_M = \mu/G$, where G is the modulus of elasticity. However, it also renders the drop capable of sustaining elastic shear waves. Therefore, a complex wave pattern reflecting off of the drop interface is formed inside the drop, and it has strong effects on the drop shape. A simple argument for the importance of waves is presented in Appendix B. It is argued that with increasing relaxation time, the wavelength decreases and finally becomes comparable to the drop dimension, leading to internal resonance. This internal wave resonance is different from the resonance discussed above in relation to the surface deformation. However, the effect of the internal wave field is felt in the surface deformation. Future analytical work will be devoted towards a detailed exposition of the phenomenon.

For polymer rheology, it is important to note that in a typical time dependent flow, a blob of polymer along with the long-chain molecules in it experiences a complex unsteady flow similar to the one studied here. Accordingly, the drop experiences retardation in stretching due to rotation of the flow field, even though the steady linear flow experiments would predict a larger stretch. Large drops in an emulsion could experience the finite Reynolds number effects mentioned here.

Acknowledgements

Appendix A

In [1] we have presented a simple harmonic oscillator model that explained most of the characteristic features of the numerical solution including different asymptotic scalings and the resonance phenomenon. In fact it also predicted the results obtained by unsteady Stokes solution in [2]. Here we extend the model to Maxwell fluid.

At the outset we briefly repeat the model for a Newtonian fluid. The deformation of a drop due to an external flow at a finite Reynolds number can be modeled as a damped mass spring system with mass $\hat{p}\hat{a}^3$, damping B, $\hat{\mu}$, and interfacial tension $\hat{T}$

$$\hat{p}\hat{a}^3\ddot{X} + \hat{\mu}\hat{a}\dot{X} + \hat{\sigma}X = \hat{\mu}\hat{a}G_0g(t) + \hat{p}\hat{a}^3G_0g(t), \qquad \dot{X}(0) = G_0g(0), X(0) = 0, \tag{A.1}$$

where ˆ has been used to differentiate the model variables from their real counterparts.

The first forcing term corresponds to the viscous stress $\mu\dot{\gamma}$. The second term represents that due to pressure (from the momentum equation, $\rho\partial u/\partial t \sim \nabla p$, one can see that a time dependent velocity $G_0g(t)$ will give rise to such a pressure). Note that G_0 is the magnitude of time-dependent shear. The initial conditions reflect an undeformed drop moving with the imposed flow velocity. For a drop having density $\rho^* = \lambda_\rho\rho$, and viscosity $\mu^* = \lambda\mu$, different from that of the continuous phase, the mass and the

damping terms in the above equations are modified by factors $(1 + \lambda_\rho)/2$ and $(1 + \lambda)/2$, respectively. Note these factors reduce to unity for identical material properties in two phases. By scaling length by $\hat{a}$ and time by $\hat{a}/G_0$ we obtain

$$\frac{(1 + \lambda_\rho)}{2} \hat{Re} \, \ddot{X} + \frac{(1 + \lambda)}{2} \dot{X} + \hat{k} X = g(t) + \hat{Re} \, \dot{g}(t), \quad \dot{X}(0) = g(0), X(0) = 0, \tag{A.2}$$

where $\hat{Re} = \frac{\hat{\rho} \hat{a} G_0}{\hat{\mu}}$ and $\hat{k} = \hat{\sigma}/(\hat{\mu} G_0)$ are the Reynolds number and inverse capillary number of the model problem, respectively. Note that the pressure forcing is absent for Stokes flow ($\hat{Re} = 0$).

For a viscoelastic drop, specifically, of a Maxwell fluid, stress is given by Eqs. (3.3) and (3.4), which on linearization and scaling obtains

$$\hat{Wi} \, \frac{\partial \tau}{\partial t} + \tau = 2\mu^* \varepsilon, \tag{A.3}$$

inside the drop. Assuming time periodicity for all dependent variables $\sim \exp(i \, \hat{St} \, t)$ ($\hat{St}$ is the model Strouhal number), we obtain

$$(i \, \hat{Wi} \, \hat{St} + 1)\tau = 2\mu^* \varepsilon \tag{A.4}$$

where $\hat{Wi}$ is the Weissenberg number. One can interpret the above relation for the drop as a constitutive equation with a complex viscosity $\mu^*/(i \, \hat{Wi} \, \hat{St} + 1)$. This consideration replaces λ in the present model equation by $\lambda/(i \, \hat{Wi} \, \hat{St} + 1)$.

Therefore, for the above ODE model, once a similar periodic variation $X = \tilde{X} \exp(i \, \hat{St} \, t)$ is assumed, for the long-time periodic solution we obtain

$$\tilde{X} = \frac{1 + i \, \hat{St} \, \hat{Re}}{-(1/2)(1 + \lambda_\rho)\hat{St}^2 \, \hat{Re} + (i/2)(1 + (\lambda/(1 + i \, \hat{Wi} \, \hat{St}))) \, St + \hat{k}}. \tag{A.5}$$

For $\hat{Wi} = 0$, we obtain the damped oscillator for a purely viscous drop, showing the resonance phenomenon observed and described in [1,2]. For a viscoelastic drop, with non-zero $\hat{Wi}$ the damping term due to the drop becomes complex. The denominator could be written separating the real and the imaginary parts

$$\left[-\frac{1}{2}(1 + \lambda_\rho)\hat{St}^2 \, \hat{Re} + \hat{k} + \frac{\lambda \, \hat{Wi} \, \hat{St}^2}{2(1 + \hat{Wi}^2 \, \hat{St}^2)} \right] + i \left[\frac{\hat{St}}{2} \left(1 + \frac{\lambda}{1 + \hat{Wi}^2 \, \hat{St}^2} \right) \right], \tag{A.6}$$

clearly showing that the viscoelasticity contributes to both damping and the spring term. It decreases damping in the imaginary part; in fact in the limit of $\hat{Wi} \to \infty$, one can see from Eq. (A.5) that the term involving λ disappears indicating that the drop damping vanishes. Therefore, the response would increase from the case of $\hat{Wi} = 0$. However, in the intermediate range the effect of viscoelasticity is complex, for it also increases spring constant in the real part. Note that for small $\hat{Wi}$, the first-order effect is only a linear increase in spring constant. However, as is also evident from the expression this viscoelastic spring constant goes to zero for large enough $\hat{Wi}$. Note the similarity of the viscoelastic terms in Eq. (A.6) with storage and loss moduli (see for instance [55], Eq. (10.24), p. 145) for linear Maxwell models. The response, therefore, is expected to decrease initially before finally increasing with $\hat{Wi}$. However, it is not always the case due to the presence of the inertia term in the denominator. If it dominates the spring term

$\hat{k}$, the viscoelastic contribution decreases the magnitude of the real part of the denominator of Eq. (A.6) giving rise to a possible temporary increase from the purely viscous case. All these behaviors due to the delicate balance of different terms are indeed observed in the plots of the response function Eq. (A.5).

Appendix B

Viscoelasticity gives rise to shear waves in a material ([56], p. 4). In a drop with UCM constitutive relation, such waves significantly affect the dynamics. With the drop having density and viscosity ρ^* and μ^*, and the relaxation time t_M, one obtains a wave speed

$$c = \sqrt{\frac{G}{\rho^*}}, \quad G = \frac{\mu^*}{t_M}, \tag{B.1}$$

where G is the bulk modulus of rigidity. In terms of non-dimensional numbers, we obtain

$$\frac{c^2}{a^2 \dot{\gamma}^2} = \left(\frac{\lambda}{\lambda_\rho}\right) \frac{1}{Re \, Wi}. \tag{B.2}$$

Noting that the wavelength l_w is related to the frequency ω and the wave speed as $c = l_w \omega/(2\pi)$, we obtain for non-dimensional wavelength

$$\left(\frac{l_w}{a}\right)^2 = \left(\frac{2\pi}{St}\right)^2 \left(\frac{\lambda}{\lambda_\rho}\right) \frac{1}{Re \, Wi}. \tag{B.3}$$

We note that in the pure viscous limit ($t_M \to 0$), bulk modulus G and the wave speed c are infinite. From Eq. (B.3), we see that in that limit wavelength too is infinite. Wave propagation becomes important when wavelength is comparable to the dimension of the drop, i.e. $l_w/a \sim O(1)$. For a fixed St, that happens with increasing Wi and Re. To sustain a wave system inside the drop the energy is expended at the cost of drop surface deformation. On the other hand, the drop with a material boundary provides a confinement suitable for a standing wave pattern. For other parameters fixed, varying relaxation time results in varying wave speed, and thereby varying wavelength. At the matching of the circular wave pattern with the drop geometry, the system is near an internal resonance, giving rise to a increased response.

References

[1] K. Sarkar, W.R. Schowalter, Deformation of a two-dimensional drop at nonzero Reynolds number in time-periodic extensional flows: numerical simulation, J. Fluid Mech., 2000, submitted for publication.
[2] K. Sarkar, W.R. Schowalter, Deformation of a two-dimensional viscous drop in time-periodic extensional flows: analytical treatment, J. Fluid Mech., 2000, submitted for publication.
[3] G.I. Taylor, The viscosity of a liquid containing small drops of another liquid, Proc. R. Soc. A 138 (1932) 41–48.
[4] G.I. Taylor, The formation of emulsions in definable fields of flow, Proc. R. Soc. A 146 (1934) 501–523.
[5] G.I. Taylor, Conical free surfaces and fluid interfaces, in: Proceedings of the 11th International Congress on Applied Mechanics, Munich, 1964, pp. 790–796.
[6] H.A. Stone, Dynamics of drop deformation and breakup in viscous fluids, Ann. Rev. Fluid Dyn. 26 (1994) 65–102.
[7] R.I. Tanner, R.R. Huilgol, On a classification scheme for flow fields, Rheol. Acta 14 (1975) 959–962.
[8] R.I. Tanner, A test particle approach to flow classification for viscoelastic fluids, AIChE J. 22 (1976) 910–918.

[9] G. Astarita, Objectivity and generally applicable criteria for flow classification, J. Non-Newtonian Fluid Mech. 6 (1979) 69–76.

[10] W.J. Olbricht, J.M. Rallison, L.G. Leal, Strong flow criteria based on microstructure deformation, J. Non-Newtonian Fluid Mech. 10 (1982) 291–318.

[11] A.J. Szeri, S. Wiggins, L.G. Leal, On the dynamics of suspended microstructure in unsteady, spatially inhomogeneous, two-dimensional fluid flows, J. Fluid Mech. 228 (1991) 207–241.

[12] B.J. Bentley, L.G. Leal, A computer-controlled four-roll mill for investigations of particle and drop dynamics in a two-dimensional linear shear flow, J. Fluid Mech. 167 (1986) 219–240.

[13] B.J. Bentley, L.G. Leal, An experimental investigation of drop deformation and breakup in steady, two-dimensional linear flow, J. Fluid Mech. 167 (1986) 241–283.

[14] J.A. Deiber, W.R. Schowalter, The potential vortex as a prototype for predictions of polymer behavior in unsteady and turbulent flows, in: Proceedings of the 11th International Congress on Rheology, Belgium, 17–21 August 1992, Elsevier, pp. 138–140.

[15] E.J. Hopfinger, F.K. Browand, Y. Gagne, Turbulence and waves in a rotating tank, J. Fluid Mech. 125 (1982) 505–534.

[16] T. Maxworthy, E.J. Hopfinger, L.G. Redekopp, Wave motions on vortex cores, J. Fluid Mech. 151 (1985) 141–165.

[17] J.M. Rallison, The deformation of small viscous drops and bubbles in shear flows, Ann. Rev. Fluid Dyn. 16 (1984) 45–66.

[18] C. Pozrikidis, Boundary Integral and Singularity Methods for Linearized Viscous Flow, Cambridge University Press, Cambridge, 1992.

[19] S.O. Unverdi, G. Tryggvason, A front-tracking method for viscous, incompressible multi-fluid flows, J. Comput. Phys. 100 (1988) 25–37.

[20] A. Esmaeeli, G. Tryggvason, Direct numerical simulations of bubbly flows. Part 1. Low Reynolds number arrays, J. Fluid Mech. 377 (1998) 313–345.

[21] A. Esmaeeli, G. Tryggvason, Direct numerical simulations of bubbly flows. Part 2. Moderate Reynolds number arrays, J. Fluid Mech. 385 (1999) 325–358.

[22] F. Dupret, J.M. Marchal, M.J. Crochet, On the consequence of discretization errors in the numerical calculation of viscoelastic flow, J. Non-Newtonian Fluid Mech. 18 (1985) 173–186.

[23] D.D. Joseph, M. Renardy, J. Saut, Hyperbolicity and change of type in the flow of viscoelastic fluids, Arch. Rational Mech. Anal. 87 (1985) 213–251.

[24] J.M. Marchal, M.J. Crochet, A new mixed finite element for calculating viscoelastic flow, J. Non-Newtonian Fluid Mech. 26 (1987) 77–114.

[25] R.C. King, M.R. Apelian, R.C. Armstrong, R.A. Brown, Numerically stable finite element techniques for viscoelastic calculations in smooth and singular geometries, J. Non-Newtonian Fluid Mech. 29 (1988) 147–216.

[26] D. Rajagopalan, R.C. Armstrong, R.A. Brown, Finite element methods for calculations of steady, viscoelastic flow using constitutive equations with a Newtonian viscosity, J. Non-Newtonian Fluid Mech. 36 (1990) 159–192.

[27] J. Sun, R.I. Tanner, Computation of steady flow past a sphere in a tube using a PTT integral model, J. Non-Newtonian Fluid Mech. 54 (1994) 379–403.

[28] J. Sun, N. Phan-Thien, R.I. Tanner, An adaptive viscoelastic stress splitting scheme and its applications: AVSS/SI and AVSS/SUPG, J. Non-Newtonian Fluid Mech. 65 (1996) 75–91.

[29] J. Sun, R.C. Armstrong, R.A. Brown, Finite element method for computation viscoelastic flows based on the discrete adaptive viscoelastic stress splitting and the discontinuous Galerkin method: DAVSS-G/DG, J. Non-Newtonian Fluid Mech. 86 (1999) 281–307.

[30] H. Hu, D.D. Joseph, Numerical simulation of viscoelastic flow past a cylinder, J. Non-Newtonian Fluid Mech. 37 (1990) 347–377.

[31] J.Y. Yoo, Y. Ng, A numerical study of the planar contraction flow of a viscoelastic fluid using the SIMPLER algorithm, J. Non-Newtonian Fluid Mech. 39 (1991) 89–106.

[32] M.S. Darwish, J.R. Whiteman, Numerical modeling viscoelastic liquids using a finite volume method, J. Non-Newtonian Fluid Mech. 45 (1992) 311–337.

[33] G.P. Sasmal, A finite volume approach for calculation of viscoelastic flow through an abrupt axisymmetric contraction, J. Non-Newtonian Fluid Mech. 56 (1995) 15–47.

[34] K.A. Missirilis, D. Assimacopoulos, E. Mitsoulis, A finite volume approach in the simulation of viscoelastic expansion flows, J. Non-Newtonian Fluid Mech. 78 (1998) 91–118.

[35] S.V. Patankar, Numerical Heat Transfer and Fluid Flow, Hemisphere, New York, 1980.

[36] P.J. Oliveira, F.T. Pinho, G.A. Pinto, Numerical simulation of non-linear elastic flows with a general collocated finite volume method, J. Non-Newtonian Fluid Mech. 79 (1998) 1–43.

[37] G. Mompean, M. Deville, Unsteady finite volume simulation of Oldroyd-B fluid through a three-dimensional planar contraction, J. Non-Newtonian Fluid Mech. 72 (1997) 253–279.

[38] D.W. Bousefield, R. Keunings, M.M. Denn, Transient deformation of an inviscid inclusion in a viscoelastic extensional flow, J. Non-Newtonian Fluid Mech. 27 (1988) 205–221.

[39] S. Ramaswamy, L.G. Leal, The deformation of a viscoelastic drop subjected to steady uniaxial extensional flow of a Newtonian fluid, J. Non-Newtonian Fluid Mech. 85 (1999) 127–163.

[40] S. Ramswamy, L.G. Leal, The deformation of a Newtoniak drop subjected to steady aniaxial extensional flow of a viscvelastic liquid, J. Non-Newtonian Fluid Mech. 88 (1999) 147–172.

[41] E.M. Toose, B.J. Geurts, J.G.M. Kueten, A boundary integral method for two-dimensional (non)-Newtonian drops in slow viscous flow, J. Non-Newtonian Fluid Mech. 60 (1995) 129–154.

[42] J.D. Jackson, Classical Electrodynamics, Wiley, New York, 1975.

[43] C. Peskin, Numerical analysis of blood flow in the heart, J. Comput. Phys. 25 (1977) 220–252.

[44] I. Stakgold, Green's Function and Boundary Value Problems, Wiley, New York, 1979.

[45] R. Peyrot, M. Taylor, Computational Methods for Fluid Dynamics, Springer, Heidelberg, 1986.

[46] C.R. Easton, Homogeneous boundary conditions for pressure in the MAC method, J. Comput. Phys. 9 (1972) 375–379.

[47] M.G.N. Perera, K. Walters, Long-range memory effects in flows involving abrupt changes in geometry part I: flows associated with L-shaped and T-shaped geometries, J. Non-Newtonian Fluid Mech. 2 (1977) 49–81.

[48] X. Huang, N. Phanthien, R.I. Tanner, Viscoelastic flow between eccentric rotating cylinders: unstructured control volume method, J. Non-Newtonian Fluid Mech. 64 (1996) 71–92.

[49] K. Goda, A multistep technique with implicit difference schemes for calculating two-or three-dimensional cavity flows, J. Comput. Phys. 30 (1979) 76–95.

[50] J. Kim, P. Moin, Application of a fractional-step method to incompressible Navier–Stokes equations, J. Comp. Phys. 59 (1985) 308–323.

[51] G. Karniadakis, M. Israeli, S. Orszag, High-order splitting methods for the incompressible Navier–Stokes equations, J. Comput. Phys. 97 (1991) 414–443.

[52] J.B. Perot, An analysis of the fractional step method, J. Comput. Phys. 108 (1993) 51–58.

[53] J.H. Ferziger, M. Peric, Computational Methods for Fluid Dynamics, Springer, Heidelberg, 1996.

[54] J.T. Davies, E.K. Rideal, Interfacial Phenomena, Academic Press, New York, 1963.

[55] W.R. Schowalter, Mechanics of Non-Newtonian Fluids, Pergamon Press, Oxford, 1978.

[56] D.D. Joseph, Fluid dynamics of viscoelastic liquids, in: Applied Mathematical Sciences, Vol. 84, Springer, New York, 1990.